Article

Cell Reports

Volume EM Reconstruction of Spinal Cord Reveals Wiring Specificity in Speed-Related Motor Circuits

Graphical Abstract

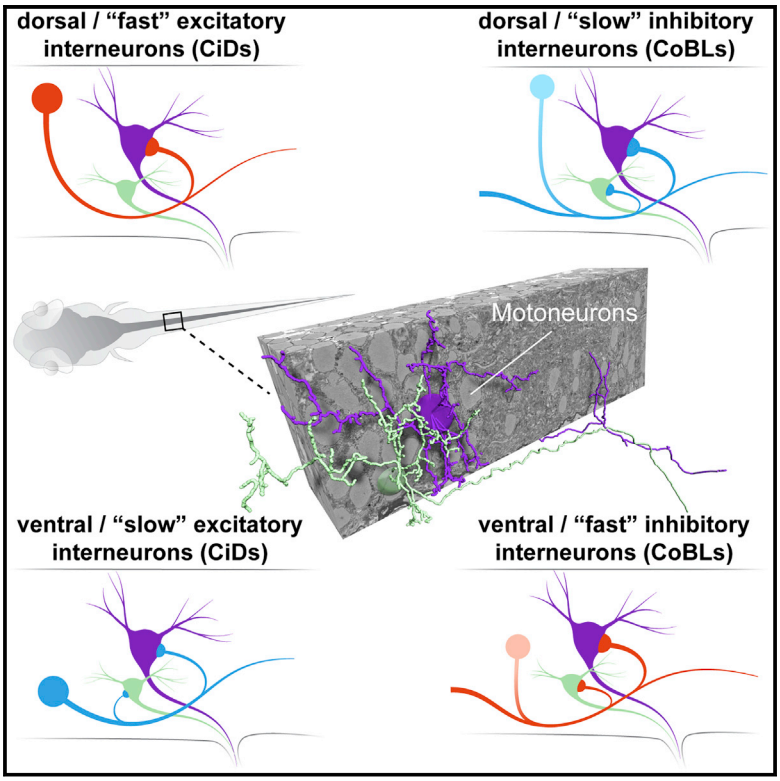

Highlights

- Serial block-face electron microscopy dataset from larval zebrafish spinal cord
- All motoneurons (MNs) in one hemisegment reconstructed, showing three subtypes
- Specific connections from "fast-swim" interneurons (displaced CiDs) to large MNs
- No speed-dependent MN specificity for commissural interneurons (CoBLs)

Authors

Fabian N. Svara, Jörgen Kornfeld, Winfried Denk, Johann H. Bollmann

Correspondence

svara@neuro.mpg.de (F.N.S.), johann.bollmann@bio.uni-freiburg.de (J.H.B.)

In Brief

Svara et al. use a three-dimensional electron microscopic dataset of larval zebrafish spinal cord to show that one type of interneuron (CiD), which drives MNs rhythmically, is partially selective in which motoneuron subtypes it contacts. This can explain mechanisms of orderly recruitment of MNs.

Svara et al., 2018, Cell Reports *23*, 2942–2954
June 5, 2018
https://doi.org/10.1016/j.celrep.2018.05.023

CellPress

OPEN ACCESS
CellPress

Cell Reports
Article

Volume EM Reconstruction of Spinal Cord Reveals Wiring Specificity in Speed-Related Motor Circuits

Fabian N. Svara,[1,2,*] Jörgen Kornfeld,[1] Winfried Denk,[1] and Johann H. Bollmann[1,3,4,*]
[1]Department of Electrons – Photons – Neurons, Max Planck Institute of Neurobiology, 82152 Martinsried, Germany
[2]Present address: Department of Computational Neuroethology, Research Center Caesar, 53175 Bonn, Germany
[3]Present address: Heisenberg Research Group, Institute of Biology I, University of Freiburg, 79104 Freiburg, Germany
[4]Lead Contact
*Correspondence: svara@neuro.mpg.de (F.N.S.), johann.bollmann@bio.uni-freiburg.de (J.H.B.)
https://doi.org/10.1016/j.celrep.2018.05.023

SUMMARY

Spinal interneurons coordinate the activity of motoneurons to generate the spatiotemporal patterns of muscle contractions required for vertebrate locomotion. It is controversial to what degree the orderly, gradual recruitment of motoneurons is determined by biophysical differences among them rather than by specific connections from presynaptic interneurons to subsets of motoneurons. To answer this question, we mapped all connections from two types of interneurons onto all motoneurons in a larval zebrafish spinal cord hemisegment, using serial block-face electron microscopy (SBEM). We found specific synaptic connectivity from dorsal but not from ventral excitatory ipsilateral interneurons, with large motoneurons, active only when strong force is required, receiving specific inputs from dorsally located interneurons, active only during fast swims. By contrast, the connectivity between inhibitory commissural interneurons and motoneurons lacks any discernible pattern. The wiring pattern is consistent with a recruitment mechanism that depends to a considerable extent on specific connectivity.

INTRODUCTION

Controlling the speed of locomotion requires controlling the frequency and force of rhythmic muscle contractions. A fundamental principle of controlling force output is that motor units are recruited in an orderly manner, with only weak units active during slow movements and stronger ones being progressively added to the active pool as faster movements require more force (Henneman et al., 1965). Although evidence for orderly recruitment has been found in many model systems (Denny-Brown and Pennybacker, 1938; Zajac and Faden, 1985; McLean et al., 2007; Ampatzis et al., 2013), less is known about how it is implemented in the spinal circuitry.

Motoneurons (MNs) driving stronger muscle fibers have larger somata (Burke et al., 1982; Ulfhake and Kellerth, 1982) and differ from weaker MNs in their active and passive membrane properties (Fleshman et al., 1981; Gustafsson and Pinter, 1984; Meneliaou and McLean, 2012), with larger MNs being less excitable so that they require more synaptic current to initiate an action potential. Consequently, an early but influential model predicted that even if the wiring between the input neurons and the MNs was completely unselective, recruitment could be staggered as long as there was a gradient in intrinsic membrane properties among MNs and the overall input activity increased monotonically with strength (Henneman et al., 1965). However, in some cases the order of MN activation depends on how the behavior is elicited (Kanda et al., 1977), which is incompatible with a mechanism based only on an excitability gradient and instead suggests that at least some of the wiring is specific (Burke, 1979). This is further supported by recordings, made in zebrafish varying in age between juvenile and adult, showing that there are strong synaptic connections between interneurons (INs) and MNs that are recruited at similar speeds (Ampatzis et al., 2014; Song et al., 2016). A comprehensive anatomical analysis is, however, lacking.

The laterally anti-phasic, rhythmic motor activity required for swimming and walking (Grillner, 2006; Goulding, 2009; Roberts et al., 2010; Kiehn, 2016) is generated by a central pattern generator (CPG) implemented by a network of spinal INs. A common morphologically identifiable IN type in fish comprises the ipsilateral, circumferential descending INs (CiDs) (Bernhardt et al., 1990), almost all of which are of the (genetically defined) V2a type (Kimura et al., 2006). V2a cells provide direct rhythmic excitation to MNs in both mouse and zebrafish spinal cord (Kimura et al., 2006; Dougherty and Kiehn, 2010; Stepien et al., 2010). At least in zebrafish, they are heterogeneous in that different V2a cells become active at different swimming speeds (McLean et al., 2008; Ampatzis et al., 2014), and activation of these cells alone is sufficient to drive swimming (Ljunggren et al., 2014).

A major question remains, however: how is the speed-dependent change of activity in a population of excitatory INs, such as the V2a cells, mapped onto the population of MNs, so that MNs are cumulatively recruited when swim speed increases? In juvenile zebrafish, V2a cells exhibit a cumulative recruitment behavior very similar to that of the MNs, with strong synaptic connections between those V2a cells and MNs that have similar recruitment characteristics (Ampatzis et al., 2014). This suggests a specific, one-to-one connectivity between V2a subtypes and MN subtypes. On the other hand, in larval zebrafish, V2a/CiD cells do not exhibit cumulative recruitment. Instead, one finds different V2a/CiD populations, each with its own, nearly

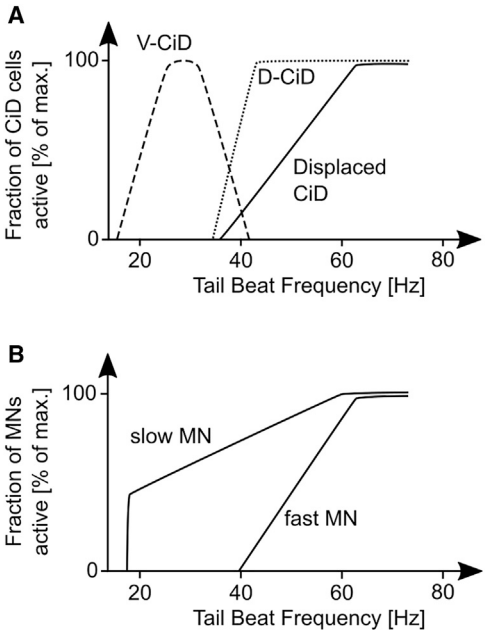

Figure 1. Physiology and Proposed Wiring Diagrams

(A and B) Schematic depiction of activity versus swim speed for (A) different CiD subtypes and (B) different MN types, on the basis of published activity measurements.

(C and D) Schematic depiction of CiD-to-MN connectivity for unspecific connectivity (C) and a model assuming partial specificity (D).

exclusive range of swim frequencies over which it is active. Ventrally and dorsally located V2a/CiDs are active only at, respectively, low and high swim speeds (McLean et al., 2008). A simple one-to-one connectivity, in this case between V2a/CiD and MN subtypes, predicts that MNs active at low speeds should stop firing at high speeds, which is in conflict with the cumulative recruitment of MNs observed experimentally (McLean et al., 2008). Different possible IN-MN connectivity patterns are, however, difficult to distinguish without comprehensive synaptic-connectivity data.

To obtain such connectivity data, we acquired a dataset from larval spinal cord using serial block-face electron microscopy (Denk and Horstmann, 2004). First, we reconstructed all MNs in one spinal segment and found three groups that could be distinguished by soma size. We then mapped connections that MNs receive from CiD and from commissural bifurcating longitudinal axon (CoBL) INs. CoBLs possess an anatomical structure that is well suited to provide rhythmic, anti-phasic inhibition that ensures that contractions alternate between both sides of the tail (Liao and Fetcho, 2008). The wiring patterns we found—strongly variable with the dorsoventral position of connected CiDs and MNs and a lack of any dorsoventral structure for CoBL-to-MN connections—are consistent with the functional roles presumed for CiDs and CoBLs in controlling locomotion.

RESULTS

Differential Patterns of CiD IN and MN Recruitment

In larval zebrafish, different CiD populations are active at different swim speeds (McLean et al., 2007, 2008). Ventral CiDs (V-CiDs) fire only at low swim speeds (<40 Hz), while dorsal CiDs (D-CiDs) and displaced CiDs, both dorsally located, fire at higher speeds (>40 Hz). Although D-CiDs quickly reach their maximal firing rate, displaced CiD activity increases gradually (Figure 1A). MNs also vary in their activity onset with dorsoventral position (McLean et al., 2007, 2008) (Figure 1B). In contrast to V-CiDs, for which the activity decreases for swim speeds >40 Hz, the activity of MNs monotonically increases with swim speed. Only the latter is consistent with cumulative recruitment. In addition to an all-to-all (unspecific) connectivity (Henneman et al., 1965), for which the recruitment order is determined solely by firing thresholds (Figure 1C), a partially specific pattern has also been considered recently (Menelaou et al., 2014) (reviewed in McLean and Dougherty, 2015). In the latter, the most dorsal CiDs, which are maximally recruited only at the fastest swim speeds, contact MN subtypes broadly, whereas more ventral CiDs, active at slower speeds, contact only ventral MNs (Figure 1D). In larval zebrafish, the range of swim frequencies in which a CiD or an MN is active can be inferred from the dorsoventral position of its cell body. This allows the translation of an anatomical wiring map into a pattern of synaptic connectivity between functional groups. This in turn reveals whether such connectivity can explain the observed recruitment patterns for MNs along the swim-speed axis.

SBEM Stack

We acquired a serial block-face electron microscopy (SBEM) stack about half way down the spinal cord, comprising two full segments flanked by two partial segments (51% and 71% of the rostrally and caudally adjoining segments, respectively), from a 6 day post-fertilization (6 dpf) larval zebrafish (Figures 2A and 2B). This region from the middle of the spinal cord at the level of the anal pore is also where most physiological recordings from spinal neurons have been performed (Buss and Drapeau, 2001; Masino and Fetcho, 2005; Wyart et al., 2009). The SBEM volume ($74 \times 74 \times 207\ \mu m^3$, at a voxel size of $9 \times 9 \times 21\ nm^3$) contained 2,177 somata, with 671 and 652 in the first and second fully contained segments, respectively. We could easily identify key features of the spinal cord anatomy, such as the ventral roots (Figures 2C and 2D) and resolve the individual neurites of the densely packed lateral neuropil (Figure 2E). We next set out to reconstruct MNs and INs and their synaptic connections.

The MNs

We began by reconstructing all MNs in the more caudal one of the two fully contained segments. We took advantage of the

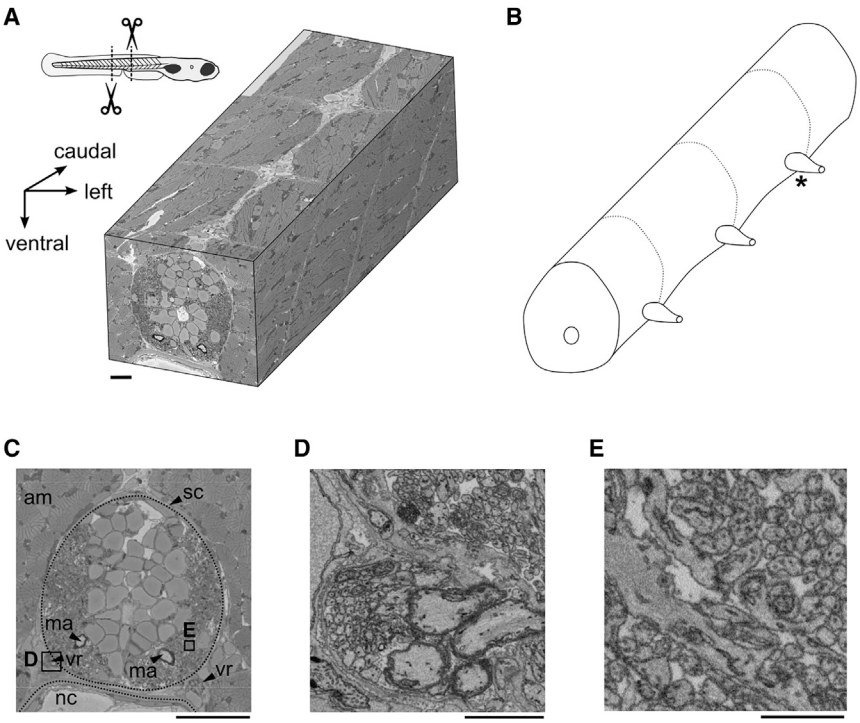

Figure 2. SBEM Volume of Zebrafish Spinal Cord

(A) Three-dimensional EM volume comprising two complete segments from central spinal cord and two partial, adjacent segments. Schematic larval zebrafish shows the location of tissue sampling.

(B) Schematic of spinal cord volume contained in the dataset. Dashed lines indicate approximate extent of spinal cord segments. Asterisk indicates the level of the pair of ventral roots from which MNs were reconstructed.

(C) Transversal overview. am, axial musculature; ma, Mauthner axon; nc, notochord; sc, spinal cord; vr, ventral root.

(D) Four large myelinated axons and many smaller unmyelinated axons exiting through a ventral root. Area as indicated in (C).

(E) Densely packed neurites in the lateral neuropil. Area as indicated in (C).

Scale bars: (C) 20 μm, (D) 2 μm, and (E) 1 μm.

fact that all MN axons exit the spinal cord through the ventral roots (VRs) and traced MNs from seed points placed in each axon passing through either the left or the right VR (Figure 3A). The left and right hemisegments contained 68 and 71 MNs, respectively (Data S1), in agreement with the highest MN counts per hemisegment previously reported for larvae (Asakawa et al., 2013). In addition, we identified all synaptic input locations on the 68 MNs in the left hemisegment, of which there were 8,528 in total.

The distribution of MN soma diameters showed two clear bumps, each approximately normally distributed (at 5.0 and 5.9 μm) and a long tail on the large diameter side (Figure 3B). The MNs in these groups were also distinguishable by (1) the size of the dendritic tree, (2) whether the axon bifurcated after leaving the spinal cord, and (3) whether the axon was myelinated. Taking these features together, all MNs could be unambiguously assigned to one of three groups.

The cells with the smallest somata (5.0 ± 0.1 μm, mean ± SD, 55 cells; Figure 3B) had either no dendrites or very short ones (longest path length 21.8 μm, 3.8 ± 4.6 μm, mean ± SD, including zero-length dendrites; Figure 3D), and they received little synaptic input (Figure 3C). Their axons did not bifurcate and were not myelinated. A large fraction of MNs (40%) were of this type (28 MNs in the left and 27 MNs in the right hemisegment). Of the 28 MNs on the left side, 22 MNs received synaptic contacts with an average count of 5.0 ± 4.1 (mean ± SD) synapses (Figure 3C), while six MNs did not receive any contact at all. This suggests that MNs in this group are in the process of being integrated into the network with only some of them already participating in the active circuitry for locomotion at this age.

The next group, medium MNs (MMNs), with somata of medium size (diameter 5.9 ± 0.3 μm, mean ± SD, 68 cells; Figure 3B), had substantial dendritic trees (total path length 172.5 ± 46.5 μm, mean ± SD, 68 cells; Figure 3D) and received considerable synaptic input (Figure 3C). Their axons did not bifurcate but instead veered either ventrally or dorsally after emerging from the VR, and were not myelinated. Of all MNs, 49% were of this type (32 MNs in the left and 36 MNs in the right hemisegment). The 32 MNs in this group on the left side had 170.4 ± 66.4 (mean ± SD) synaptic inputs per cell (Figure 3C).

Large MNs (LMNs) had soma diameters greater than 6.5 μm (7.7 ± 0.8 μm, mean ± SD, 16 cells; Figure 3B), even bigger dendritic trees (path length 271.2 ± 71.7 μm, mean ± SD, 16 cells; Figure 3D) and numerous synaptic inputs (370.9 ± 23.0 synapses, mean ± SD, 8 cells on the left side; Figure 3C). Eight cells (4 on each side) had unmyelinated, bifurcating axons, and another 8 cells (4 on each side) had non-bifurcating axons that were myelinated. The somatic positions and axonal trajectories of the myelinated cells indicate that they are the early born primary MNs (PMNs), individually identifiable as CaP (caudal primary), MiP (middle primary) and v-RoP and d-RoP (ventral and dorsal rostral primary) (Data S1, cells 1–4 and 69–72) (Myers et al., 1986; Menelaou and McLean, 2012).

Although the somata of the different groups are segregated (LMNs more dorsal and MMNs more ventral; Figure 3B) their neurite distributions overlap (Figures 3E–3G), which is consistent both with models that call for specific wiring and for models that do not. To distinguish between these models, a more detailed analysis of the connections between INs and MNs is needed.

Identification of CiD INs

Next, we set out to identify CiDs because the vast majority of these in larval zebrafish at 4–5 dpf are excitatory V2a-type INs (Kimura et al., 2006). CiDs are morphologically distinct in that

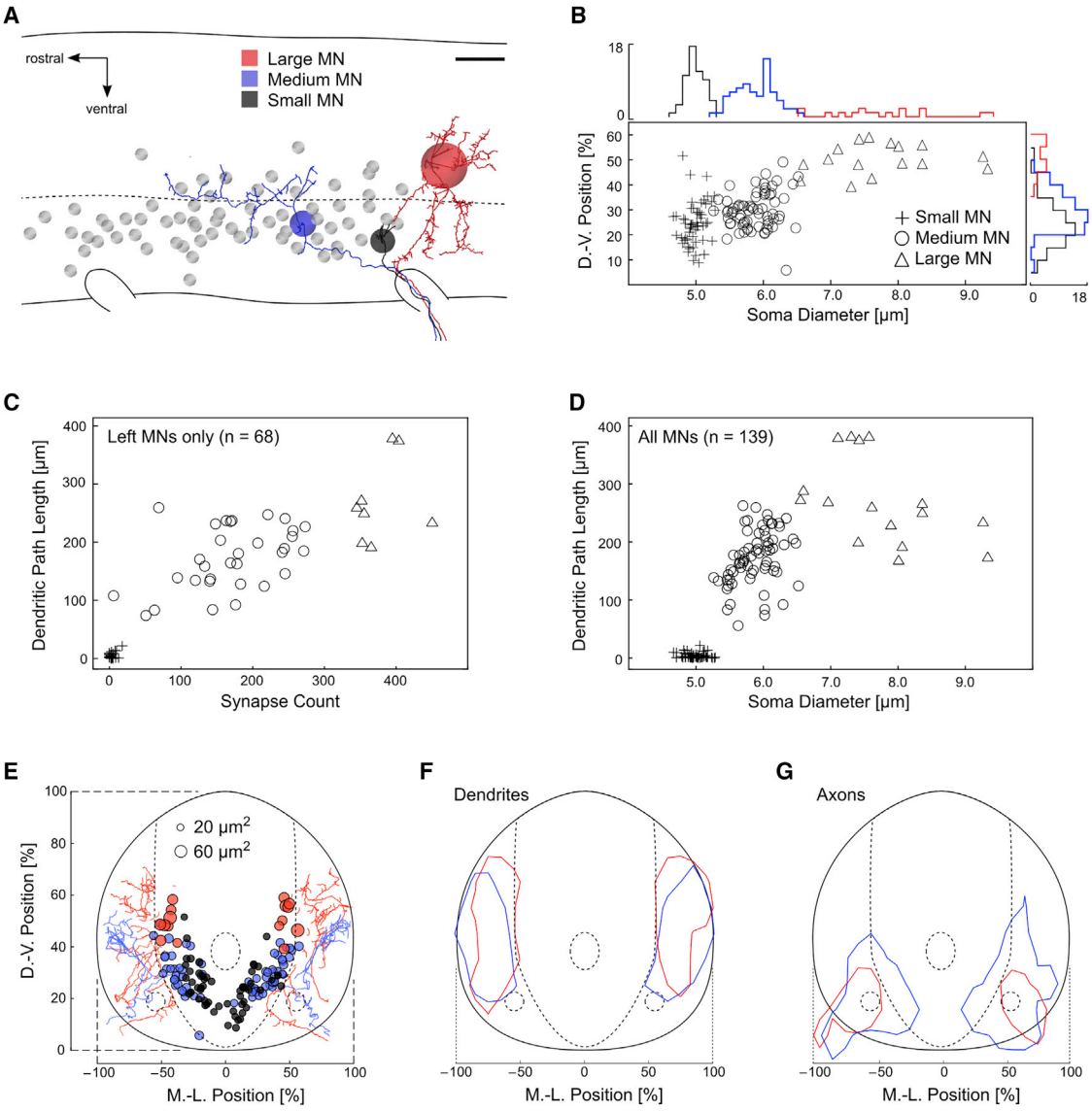

Figure 3. Motoneuron Reconstruction and Classification

(A) A large MN (the CaP MN, red), a medium MN (blue), and a small MN (black) with axons exiting through the same ventral root (VR). Gray disks, soma locations of all other 65 MNs with axons exiting through the same VR. Dashed line, center of central canal. Scale bar: 10 μm.

(B) Dorsoventral position versus soma diameter. Above and to the right: corresponding histograms for the three different MN subtypes.

(C and D) Dendritic path length versus incoming synapse count (C) and versus soma diameter (D).

(E) Axial projection of soma locations for all 139 reconstructed MNs. Neurites of one LMN (red) and one MMN (blue) are shown on each side. Some branches and stubs appear unconnected because somata-indicating disks are smaller than actual somata.

(F) Contours indicating where the projected neurite density crosses 10% of the peak density for large MN dendrites (red) and medium MN dendrites (blue).

(G) As in (F), but for the axons.

their axons first run ventrally and then turn to run caudally for several segments (Bernhardt et al., 1990; Hale et al., 2001). Because their axons do not cross the midline, CiDs can connect only to ipsilateral MNs. To identify the CiDs among the almost 600 neurons located ipsilaterally and rostrally from the hemisegment that contained the reconstructed MNs, we relied on a human's ability to determine that a cell is not a CiD, often rather quickly after having started to trace a cell (Figures 4A–4C). A cell was rejected in any of the following cases: an axon branch (1) left the spinal cord through a VR, which only MN axons do (21% of all cells; Figure 4C), or (2) crossed the midline of the spinal cord (33% of all cells; Figure 4C), or (3) the cell had sheet-like processes, characteristic of glia (18% of the cells). Of the 170 remaining cells, each of which was completely traced, 39 had an ipsilaterally descending axon trajectory (Figures 4A–4C) that was consistent with the morphology of V2a-type CiDs (Kimura et al., 2006; Menelaou et al., 2014) (Data S2). These cells had somata located between 36% and 90% along the dorsoventral

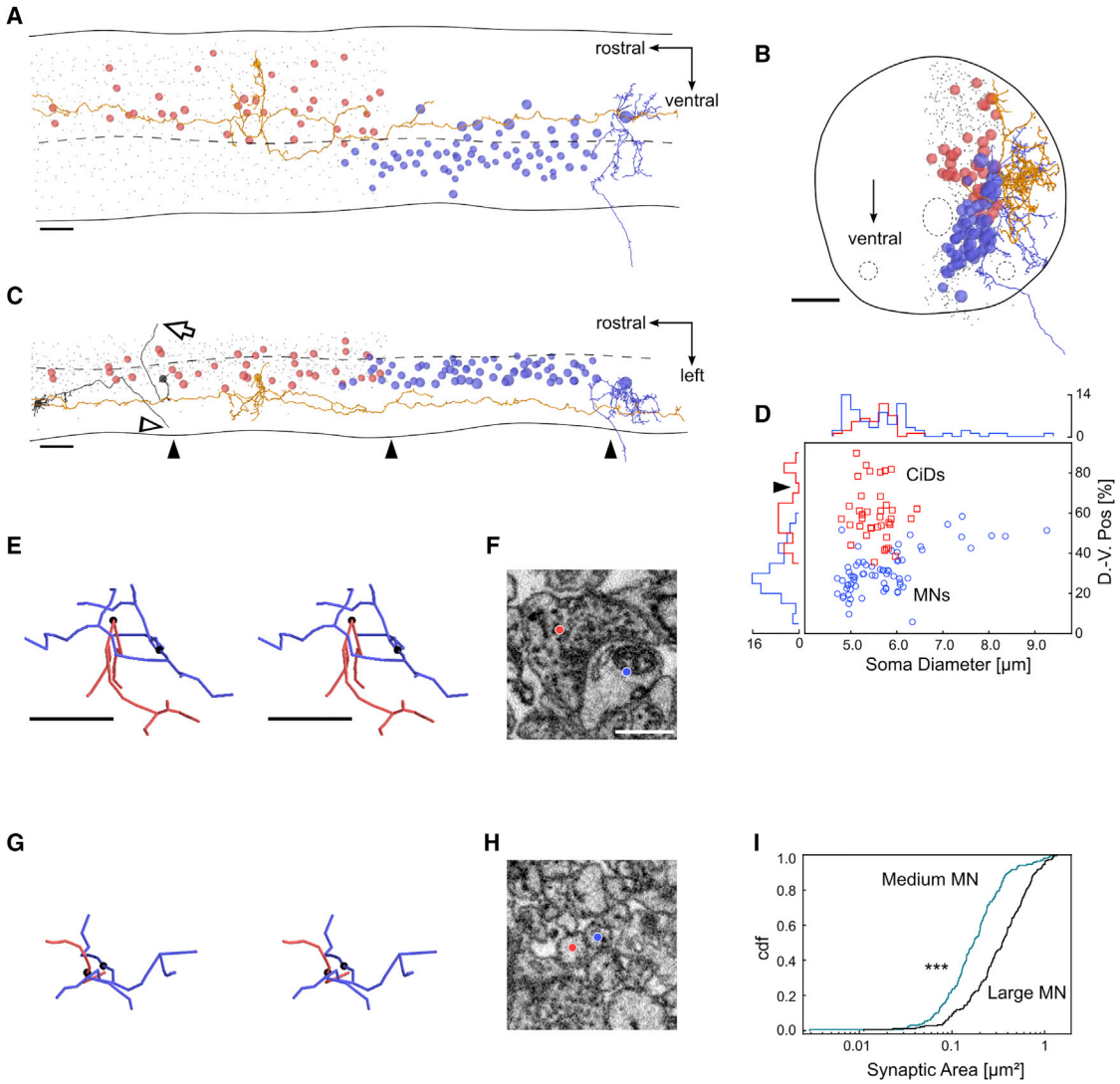

Figure 4. Reconstruction of CiD Interneurons

(A–C) Sagittal (A), axial (B), and coronal (C) projections showing one LMN (blue) and one CiD in the rostrally adjacent segment (orange), both with skeletonized neurites. Also shown are the soma locations of all reconstructed MNs on the left side of the spinal cord and of all reconstructed CiDs in the rostrally adjacent segment (blue and red disks, respectively). The diameters of the disks are equal to 40% of the actual soma diameters. Gray dots, all other soma locations in the region where CiDs were reconstructed. In addition, (C) shows two neurons (gray soma disks) for which tracing was aborted once it was determined that the cell could not be a CiD, because the axon crossed the midplane (open arrow) or passed through the VR (open arrowhead), respectively.

(D) Dorsoventral position versus soma diameter for CiDs (red squares) and MNs (blue circles). Top and left: histograms. Arrowhead points at gap between displaced and non-displaced CiDs (compare Figures 5A and 5D).

(E–H) Stereo-views of proximity location between a CiD axon (red) and an MN dendrite (blue), with (E) and without (G) an actual synapse. (F and H) corresponding cross-sections through EM data. Black spheres in (E) and (G) correspond to colored disks in (F) and (H).

(I) Distribution of individual synaptic contact areas between CiDs and MNs for large (black line) and medium (blue-gray line) MNs ($p < 0.001$, Student's t test).

Scale bars: (A)–(C) 10 μm, (E) 1 μm, and (F) 500 nm. Scale bars in (E) and (F) also apply to (G) and (H).

axis, more dorsal than most MNs (Figure 4D), in agreement with previous observations (Menelaou et al., 2014).

To identify all connections between a CiD IN and an MN, we inspected all locations where the skeleton of the CiD axon came within 1 μm of the MN's skeleton (Figures 4E–4H; see Experimental Methods). A synapse was inferred if cell membranes were parallel, at least part of the contact area showed additional darkening (a postsynaptic density), and a vesicle cloud was present and touched the presynaptic membrane (compare Figures 4E and 4F with Figures 4G and 4H). Synapses were found at 265 of 5,111 inspected locations. Individual synaptic contact areas ranged from 0.003 to 1.362 μm^2 (Figure 4I). Of the 39 CiDs, 35 made at least one synapse onto one reconstructed MN. For these 35 cells, the mean number of synapses was 7.6 ± 6.2 (mean ± SD, range 1–25). The synaptic contact area was, on average, almost twice as large for LMNs

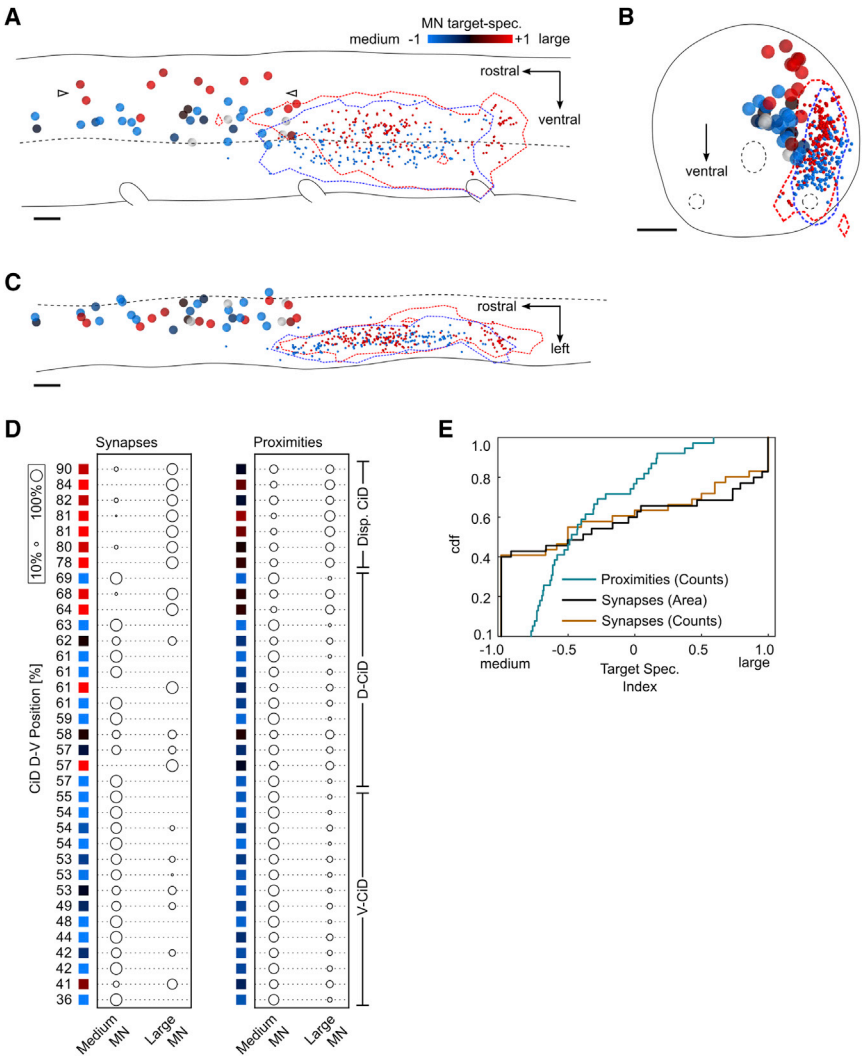

Figure 5. CiD-to-MN Connectivity

(A–C) Sagittal (A), axial (B), and coronal (C) projections of CiD somata colored by their synaptic weight-based target specificity index. Light gray, CiDs without synaptic connection onto MNs. Dashed line, center of central canal. Red and blue dotted lines, 10% density contours of LMN and MMN neurites, respectively. Small disks, locations of synapses onto LMNs (red) and MMNs (blue). Open arrowheads in (A), gap between displaced and non-displaced CiDs. Scale bars: 10 μm.

(D) Wiring between CiDs (sorted by dorsoventral position) and MN types, normalized for each CiD. Left matrix: summed synaptic areas; right matrix: proximity counts. The dorsoventral ranges for each CiD type are indicated by vertical lines on the right. Colored boxes indicate TSI, calculated using either synaptic weights (left) or proximity counts (right).

(E) CiD TSI distribution, on the basis of the synaptic area (black), number of synaptic contacts (brown), and number of proximities (blue-gray).

($0.41 \pm 0.02\ \mu m^2$, mean ± SEM, n = 127, $p < 0.001$) as for MMNs ($0.21 \pm 0.02\ \mu m^2$, mean ± SEM, n = 135) (Figure 4I). Only three synapses (0.07, 0.13, and 0.14 μm^2 in size) were made onto small MNs. We performed the subsequent analyses of CiD-to-MN connectivity with the 35 CiDs that did contact MNs.

CiD-to-MN Wiring

Having obtained the three-dimensional reconstructions of MNs and CiDs along with the synapses between them, we next analyzed their connectivity. First, we tested for each CiD whether it preferentially contacted either LMNs or MMNs using a target specificity index (TSI = [L − M]/[L + M], where L and M are the summed synaptic contact areas on LMNs and MMNs, respectively). The TSI runs from +1 (the CiD exclusively forms synapses with LMNs; Figures 5A–5D, red) to −1 (the CiDs contact only MMNs; Figures 5A–5D, blue). Relative to the median dorsoventral position of all CiDs, 10 of 11 cells with TSI > 0.6 were dorsal, and similarly, 10 of 16 CiDs with TSI < −0.6 were ventral (Figures 5A–5D). About a quarter of all CiDs (8 of 35) had no distinct preference (−0.6 < TSI < 0.6). When using the number of close encounters between skeletons instead of actual synaptic area to calculate the TSI, this fraction rose to more than half (63% [22 of 35 cells]), and none of the CiDs retained a preference for LMNs (Figures 5D and 5E). This is probably the case because LMN and MMN dendrite territories overlap substantially (Figure 3F) and MMNs outnumber LMNs, reducing the probability that an axon encounters an LMN dendrite.

To compare our findings with the assumptions made in different models of orderly MN recruitment (Figures 1C, 1D, S1, and S2), we mapped our CiD classes onto the previously described V-CiD, D-CiD, and displaced CiD classes, which are defined physiologically and differ in dorsoventral soma position and in the swim frequency dependence of their activation (Figure 1A). Of the CiDs in our dataset, seven had a dorsoventral soma position between 78% and 90% (Figures 4D and 5A–5D), while the remaining CiDs were all below 70%, consistent with earlier descriptions of a clear gap between displaced and non-displaced CiDs (Kimura et al., 2006; McLean et al., 2008). The non-displaced CiDs comprise V-CiDs, which are active mostly below 40 Hz swim frequency, and D-CiDs, active mostly above 40 Hz, which are two CiD subtypes that have been reported to be anatomically segregated along the dorsoventral axis (McLean et al., 2008). Therefore, we placed the ventral half of the non-displaced CiDs in the V-CiD group and the dorsal half in the D-CiD group (Figure 5D).

Displaced CiDs made between 86.8% and 100% of their contacts with LMNs. They appeared to avoid MMNs, with which they formed hardly any synapses despite many close encounters between their axons and MMNs (Figure 6A). In comparison, V-CiD synapses followed in their distribution that of

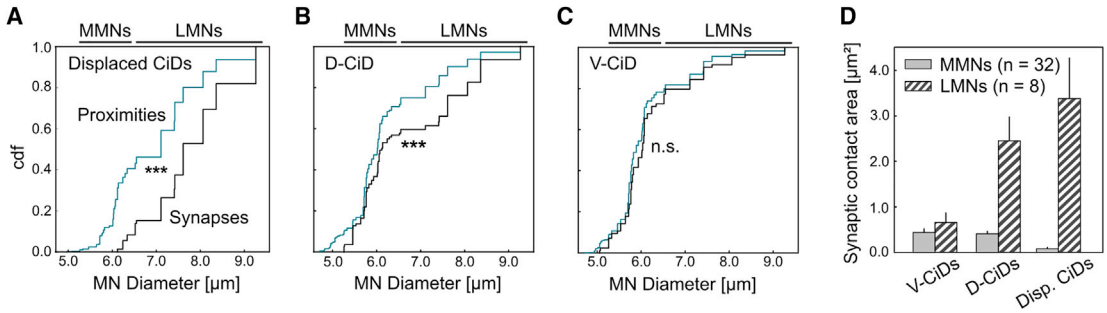

Figure 6. Specificity of CiD Inputs to MN Subtypes

(A–C) Distribution of the number of synapses (black lines) and proximity locations (blue-gray lines) onto MNs of different sizes, for (A) displaced CiDs ($p < 0.001$), (B) D-CiDs ($p < 0.001$), and (C) V-CiDs ($p = 0.27$, KS test).

(D) Average total contact area from the different CiD subtypes onto an MMN and LMN. Error bars indicate SEM.

skeleton-proximity locations (Figure 6C), while D-CiDs showed a slight preference for LMNs (Figure 6B).

To compare their relative impact, we calculated the average contact area made by the different CiD sub-populations onto an LMN and an MMN, respectively. MMNs received on average a similar amount of synaptic contact area from V-CiDs (47%) and D-CiDs (44%) but significantly less from displaced CiDs (9%) (Kruskal-Wallis-test, $p < 0.001$; Figure 6D). In contrast, LMNs received on average 52% from displaced CiDs and 38% from D-CiDs but only 10% of their synaptic contact area from V-CiDs (difference between V-CiD and displaced CiD input: $p < 0.001$, Kruskal-Wallis-test; Figure 6D). In other words, LMNs received 90% of their synaptic contact area from D-CiDs and displaced CiDs, which are presumably active only at high swim frequencies (Figure 1A). Four D-CiDs were specific for LMNs with TSIs > 0.6 (red squares among D-CiDs in Figure 5D). They contributed the majority (59%) of the contact area between D-CiDs and LMNs.

To summarize, the CiD types provided more synaptic contact area onto LMNs the further dorsal they were, with the most dorsal, displaced CiDs providing input almost exclusively to LMNs. Many cells in the dorsal half of CiDs were connected only to LMNs. These findings stand in contrast to earlier models of larval MN recruitment, which either assumed a uniformly low MN specificity across CiD subtypes (Figure 1C) or a specificity that increased along the dorsoventral axis (Figure 1D).

CoBL-to-MN Wiring

Finally, we asked whether inhibitory INs also exhibit any specificity in the MNs they contact. Inhibitory INs of the CoBL type are a class of neurons that is the leading candidate for providing rhythmic, anti-phasic contralateral inhibition during swimming (Liao and Fetcho, 2008). The activation threshold, with respect to swim speed, for CoBLs is, like that of CiDs, dependent on the dorsoventral soma position, but the dependence is inverted (i.e., a more dorsal location for a CoBL indicates activation at low swim speed, whereas more ventral ones are only active at higher speeds) (McLean et al., 2007). To identify a set of inhibitory CoBLs, we started by placing seed points in all axons that synaptically contacted either one of two different MNs, an LMN (cell 1, the CaP MN) and an MMN (cell 42 in Data S1). We traced from all seed points until we could either unambiguously determine that a cell was not a CoBL or until the cell was completely traced. We found 34 CoBLs, of which 27 contacted only the CaP, 6 contacted only cell 42, and one contacted both of them (Data S3). We then identified all synapses between the 34 CoBLs and all contralateral MNs (Figures 7A–7C) by inspecting all skeleton-proximity locations. The number of synapses each CoBL made onto the reconstructed MNs was almost twice as large (13.8 ± 1.3, mean ± SEM, range 2–40) as that for the CiDs (7.6 ± 1.1, mean ± SEM, 35 cells, $p < 0.001$). Many CoBLs contacted LMNs and MMNs without any apparent specificity, with TSIs between −0.6 and +0.6 for 18 of 34 cells (Figures 7D and 7E). CoBLs that were target specific (TSI > 0.6, 8 cells; TSI < −0.6, 8 cells) did not appear to prefer any particular dorsoventral position (Figures 7A–7D). There was also no correlation between the position of a CoBL and the number of its contacts or the total synaptic contact area with MNs (Figure S3). The distribution of TSIs based on the synaptic area between CoBLs and MMNs was more uniform than that based on proximity, which means that CoBLs have a slight preference for LMNs (Figure 7E). Similar to the CiDs, CoBL synapses onto LMNs were, on average, larger than those onto MMNs (Figure 7G). Finally, in order to test whether the speed-dependent activation threshold affected how CoBLs distribute their synaptic output among different MN types, we divided the CoBLs into three groups on the basis of the dorsoventral position of the soma and calculated the average contact area an LMN and an MMN received from these sub-groups. The average CoBL-derived synaptic contact area onto an MMN was 36% for dorsal CoBLs, 27% for central CoBLs, and 37% for ventral CoBLs, while that onto an LMN was 22% for dorsal CoBLs, 39% for central CoBLs, and 39% for ventral CoBLs, and no significant differences were detected within each MN class ($p > 0.05$, Kruskal-Wallis-test; Figure 7H). In summary, it appears that CoBL-to-MN connectivity, unlike CiD-to-MN connectivity (Figures 5 and 6), is not organized by MN class along the dorsoventral axis.

DISCUSSION

Using a SBEM dataset from larval zebrafish spinal cord, we have analyzed MN inputs from two types of spinal INs, one projecting

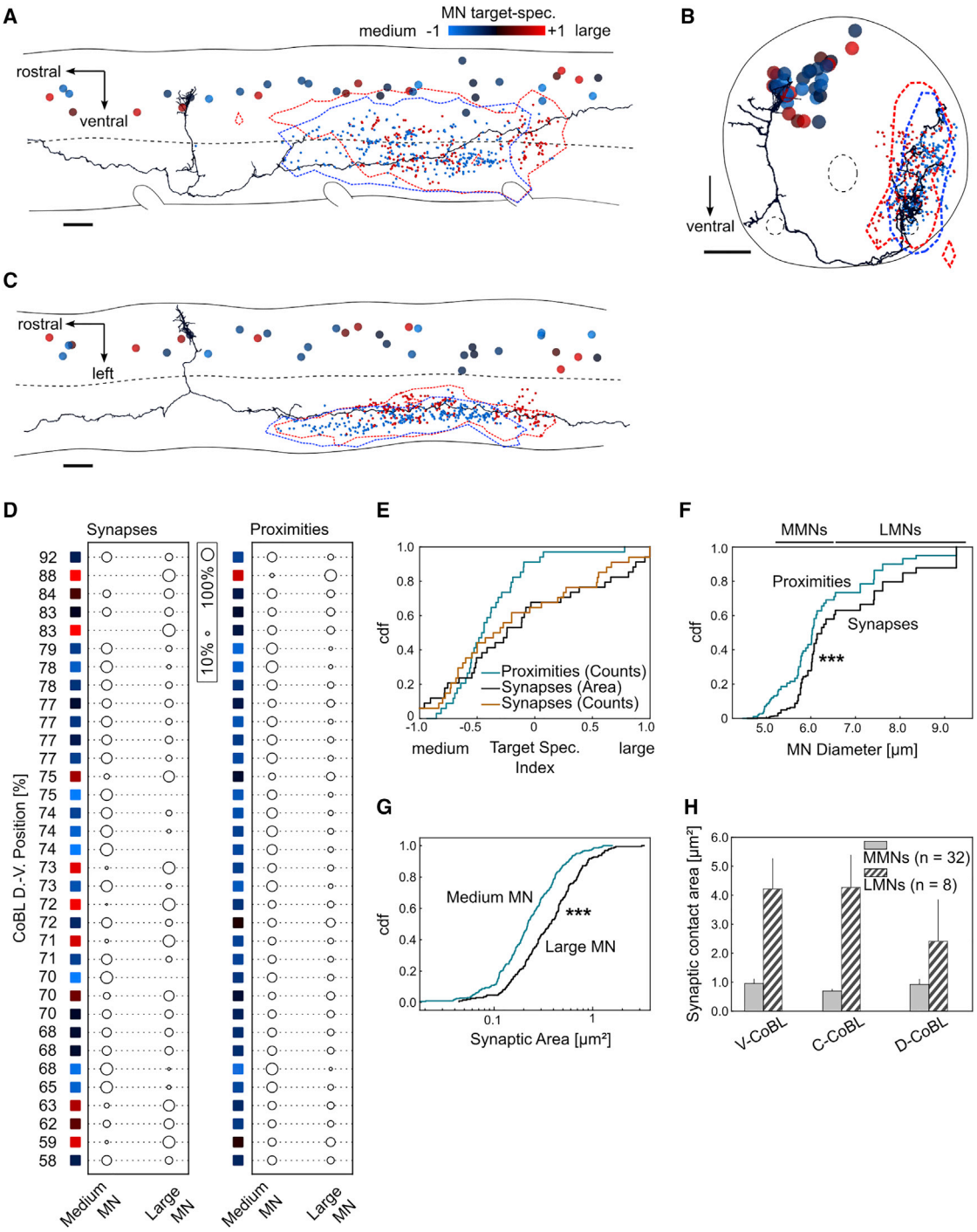

Figure 7. CoBL-to-MN Connectivity

(A–C) Sagittal (A), axial (B), and coronal (C) projections of CoBL somata colored by their synaptic weight-based target MN specificity index, including one example of a CoBL (black-blue cell). Scale bars: 10 µm.

(D) Wiring between CoBLs (sorted by dorsoventral position) and MN subtypes, normalized for each CoBL. Left matrix: summed synaptic contact area; right matrix: proximity counts. The colored boxes indicate the TSI for each cell, calculated using synapse size (left) or proximity counts (right).

(E) TSI distribution for the CoBLs, on the basis of synaptic areas (black), number of synaptic contacts (brown) and on the number of proximities (blue-gray).

(F) Distribution of the number of CoBL synapses (black line) and the number of proximity locations (blue-gray line) onto MNs of different sizes ($p < 0.001$, KS test).

(G) Distribution of individual synaptic contact areas of CoBLs onto MMNs (blue-gray line) and LMNs (black line) ($p < 0.001$, Student's t test).

(H) Average total contact area from the ventral third (V-CoBLs), central third (C-CoBLs), and dorsal third (D-CoBLs) of reconstructed CoBLs onto an MMN and LMN, respectively. Error bars indicate SEM.

ipsilaterally (the CiDs) and one commissural type (the CoBLs), and found that target specificity depended on a CiD's soma position along the dorsoventral axis (Figures 5 and 6). In particular, the specific wiring between the most dorsal CiDs and LMNs suggests that MN subtype-specific wiring plays an important role in the recruitment of the LMNs at high swim speeds. Combining the assumption that LMNs depend on those specific inputs to be active with the observation that LMNs have high firing thresholds (Menelaou and McLean, 2012) supports a model in which the recruitment order of MNs depends both on the biophysical properties of the target cell and the specificity of neural wiring. On the other hand, CoBLs, in their putative role as enforcers of bilateral alternation (Liao and Fetcho, 2008), merely need to suppress all activity on the contralateral side, which does require that all MNs are innervated but not in a specific way. Consistent with this, we failed to find any significant dorsoventral variation in MN class preference.

The MNs

MNs fall into anatomically distinguishable groups (differing in soma size, dendritic path length, and soma position along the dorsoventral (D-V) axis; Figures 3B and 3D). Because the recruitment frequency also varies along the D-V axis (McLean et al., 2008), these groups presumably correspond to functional classes, each serving a different swim-speed range. However, physiological data from larval fish show that many MN properties, such as input resistance and rheobase, vary widely but gradually, without forming discrete groups (Menelaou and McLean, 2012), suggesting that the anatomically defined classes are physiologically inhomogeneous. In the juvenile fish, by contrast, MNs form four clusters, based both on physiological and on anatomical parameters alone (Ampatzis et al., 2013), suggesting that physiological subdivisions sharpen in the course of development. Furthermore, among the large group of MMNs we did not find a further subdivision on the basis of our connectivity data. This suggests that any graded recruitment of MMNs depends on a broadly distributed excitability (e.g., because of differences in rheobase and membrane time constant).

What are the functional roles of the three different MN classes? The cells in the LMN group have in common that they are active only at swim speeds above 40 Hz (McLean et al., 2008), innervate deep, fast-twitch musculature (Menelaou and McLean, 2012), and are innervated by displaced CiDs. This indicates that there is a channel, with dedicated wiring, that synchronously activates many fast-twitch muscle fibers throughout the myotome and generates the powerful contractions needed for startle responses and escape behavior. The cells in the MMN class likely project to both deep, fast-twitch fibers and to the layer of slow-twitch fibers on the skeletal muscle surface (Menelaou and McLean, 2012; Kishore et al., 2014). MMNs were contacted mainly by non-displaced CiDs, which cover a large frequency range. This suggests that MMNs control muscle contraction over a wide range of swim speeds, at least at this developmental stage. That leaves the small MNs, which, judging by the sparsity of synaptic inputs at this developmental stage, appear to be not yet fully integrated into the circuit. They may correspond to the MNs with the highest input resistance in larval spinal cord, which preferentially contact superficial slow-twitch muscle fibers (Kishore et al., 2014). Also, the number of small MNs found here matches that of a group of MNs in older fish that contact superficial, red muscle and represent ~30 MNs per hemisegment (van Raamsdonk et al., 1983). Together, this suggests that the small MNs at this stage are in the process of forming a module of weak motor units with slow-twitch fibers, which may become important at the adult stage for slow continuous swimming.

The INs

To the extent to which models of MN recruitment in larval zebrafish assume any wiring specificity it is for low-speed CiDs only (Figure 1D). Our findings show that it is in fact a component of the high-speed circuitry made up of displaced CiDs that is specific. This is surprising but fits well with the observed activity pattern. Both displaced CiDs and the largest MNs are maximally recruited only during the fastest swims. A dedicated CiD population may be needed to drive the largest MNs, which have low input resistances, above threshold and may be the reason for the disproportionately large excitatory input current that only MNs with low input resistance receive during fast swimming (Kishore et al., 2014). The specificity of the displaced CiDs likely ensures that LMNs are activated when and only when strong muscle contractions are needed, for example for a powerful startle or escape response (Ritter et al., 2001; Burgess and Granato, 2007). LMNs, which form strong motor units, appear unsuitable for behaviors, such as prey capture, that require movement precision (McElligott and O'Malley, 2005; Bianco et al., 2011; Trivedi and Bollmann, 2013; Marques et al., 2018). The remaining (non-displaced) CiDs included cells that predominantly made synapses onto either MMNs or LMNs or onto both (Figure 5). But neither V-CiDs nor D-CiDs were, as a group, selective for any MN subtype. This connectivity can explain how sets of CiDs active at different swim speeds might lead to cumulative recruitment of MNs as the swim speed increases: V-CiDs are active at slow swim speeds and provide input to all MNs but only activate those with low spiking thresholds. At higher speeds, the V-CiDs stop firing and D-CiDs become active (Figure 1A). On the basis of our connectivity data, V-CiDs and D-CiDs have about the same synaptic weight onto the MMNs, which suggests that D-CiDs can maintain MMN activity at higher swim speeds while, in addition, providing synaptic input also to LMNs, which are known to be active only at higher speeds (Figure 6D). On the other hand, given the diffuse connectivity between V-CiDs and MMNs, it seems likely that MMNs are recruited in an order that depends on their individual firing thresholds.

Finally, the lack of speed-specific topographic order in CoBL-to-MN wiring (Figure 7) is consistent with measurements showing that anti-phasic inhibitory currents scale with swim frequency but are independent of MN input resistance and recruitment threshold (Kishore et al., 2014). This supports the view that CoBLs ensure left-right alternation by indiscriminately shutting down all MNs on the contralateral side of the spinal cord.

Inferring Neuronal Function from Morphology

We have assumed that the morphologically defined CiDs in our dataset correspond to excitatory V2a cells, which are defined genetically. This is because in larvae older than 2 dpf, only very few of the ipsilaterally descending neurons are not of the V2a

type, and the axons of those that are not run more ventral than V2a cell axons (Kimura et al., 2006). We found only three INs that had unusually ventral axons running near or below the Mauthner axon, but those INs were excluded from our analysis of CiD-to-MN wiring. Our count of 24 CiDs per hemisegment is in good agreement with counts of V2a cells in 4–5 dpf larvae (20 per hemisegment [Menelaou et al., 2014], 25 per hemisegment [Eklöf-Ljunggren et al., 2012]), which strongly supports the view that most if not all CiDs in our sample are V2a INs.

The CoBLs, on the other hand, as identified by their axonal trajectory, likely represent glycinergic V0-iB neurons from the p0 domain (Liao and Fetcho, 2008; Satou et al., 2012). There are several other IN types with commissural axons that were fully traced in the analysis of commissural projections. These, however, could be distinguished from V0-iB neurons on the basis of differences in the axonal morphology. A commissural albeit excitatory IN type, also from the p0 domain called V0-eB (Satou et al., 2012), possesses an axon that remains at a constant D-V level and forms long, dorsally directed collaterals densely distributed in segments near the bifurcation, and was excluded from further analysis. Other commissural INs are the so-called CoLA (commissural longitudinal ascending), which we did not find in our sample of commissural INs, and CoLo (commissural local) cells, which were distinguishable from CoBLs because of a myelinated axon that contacted the Mauthner axon (Hale et al., 2001; Liao and Fetcho, 2008; Satou et al., 2009). We cannot rule out that other commissural INs from other progenitor domains are also bifurcating. Commissural INs for example from the pd6 domain, which are less well characterized, could have bifurcating axons; however, many of these cells have been found to be glycinergic (Satou et al., 2013) and could therefore also provide anti-phasic inhibition to the contralateral side.

Our reconstructed volume included approximately three spinal cord segments, but CiDs can extend their axons caudally for many segments. It is therefore possible that the pattern of connectivity between CiDs and MNs separated by several segments is different from that found here in adjacent segments. However, the density of CiD axon branches appears to be highest close to the soma (Menelaou et al., 2014), suggesting that most of their synapses are made there. The volume size may also be the reason why we did not find in our back-tracing of commissural cells any multipolar commissural descending (MCoD) INs (Bernhardt et al., 1990; Hale et al., 2001), which make synapses several segments away from their somata (McLean et al., 2008). MCoDs provide excitatory input to MNs at the lowest swim frequencies (15–30 Hz), and could therefore contribute to driving MMNs, and potentially small MNs, at these frequencies. This is supported by the fact that silencing synaptic output from V2a cells shifts the distribution of swim frequencies to the very low range (Sternberg et al., 2016). To identify such far projecting neurons will require an EM-based acquisition ideally of the entire spinal cord, similar to how large-caliber myelinated projection neurons could be followed over long distances in an EM volume comprising the whole brain of a zebrafish larva (Hildebrand et al., 2017). Thus, the acquisition of a larger spinal EM volume should make it possible to map synaptic connections between all INs and MNs and to compare their connectivity across many segments, provided the section thickness is sufficiently small to enable tracking also of thin unmyelinated axons, as performed here and previously (Wanner et al., 2016). Finally, the fact that recent light microscopy-based estimates of the total number of MNs per hemisegment (Asakawa et al., 2013) and of the number and location of identifiable PMNs (Menelaou and McLean, 2012) agree well with the numbers and locations we found provides strong support that the spinal cord volume sampled here is representative of the general spinal cord anatomy at this stage.

Combining Physiological and Connectomic Data to Test Models of MN Recruitment

How do our findings help us in the search for the mechanism of force recruitment in the spinal cord? To address this question, we created a set of 4,096 models assuming three types of CiDs (V-CiDs, D-CiDs, and displaced CiDs), two types of MNs (LMNs and MMNs), and connections between CiDs and MNs that could be (1) absent, (2) weak (cannot trigger action potentials when active alone), (3) strong (can trigger action potentials alone), or (4) saturating (can trigger maximal response alone). After eliminating all models that are inconsistent with published physiological data, 294 models remained (Figure S1), but only 23 of these are also consistent with our connectivity data (Figure S2). To distinguish between the remaining models, physiological measurements of the effects of the activation of a CiD sub-population onto different MN subtypes would be required, because our anatomical measurements of synapse size do not yield an estimate of how strong a synapse is relative to the postsynaptic cell's excitability.

When comparing our results in the larval zebrafish with what is known for juvenile to adult fish, it becomes clear that in the larval fish the separate, speed-tuned microcircuit modules, as they are observed in older fish (Ampatzis et al., 2014), have not yet formed. Some major features of the mature organization (i.e., morphologically distinct MN classes and partial specificity in the fast swimming network) are, however, already present. The small MNs, which, according to our data, receive virtually no CiD input, probably become part of the slow swimming network in juvenile fish. The development from a larval, partially specific network to a highly modular one in the adult suggests that the ipsilateral excitatory IN-MN network undergoes a significant synaptic reorganization.

EXPERIMENTAL PROCEDURES

Animal Handling, Preparation, and EM Staining

A 6 dpf nacre zebrafish larva (*mitfa*$^{-/-}$; Lister et al., 1999), raised at 27°C in embryo medium on a 14/10 hr light/dark cycle, was used for SBEM. Good health was assessed by observing the successful completion of several prey capture sequences directed at paramecia immediately before the preparation. The tail of the euthanized larva was cut several segments caudal from the 15th myotome. A modified Ringer solution (63 mM NaCl, 63 mM cesium gluconate, 2.5 mM KCl, 25 mM $NaHCO_3$, 1.25 mM NaH_2PO_4, 25 mM glucose, 2 mM $CaCl_2$, and 1 mM $MgCl_2$), based on the principle of extracellular space preservation by cell-impermeable solutes (Cragg, 1980), was injected directly into the spinal cord using a sharp glass pipette, approximately five segments rostral of the cut location. Slight positive pressure was maintained using a PicoSpritzer III (Parker Hannifin) to ensure continuous flow of the solution through the spinal cord and out through the cut for 2 min. The tail was then cut off at the injection location and prepared for electron microscopy as previously

described (Briggman et al., 2011). Experiments were in accordance with the guidelines of the German animal welfare law and the local government (Regierungspräsidium Karlsruhe).

SBEM Acquisition and Image Alignment

SBEM image acquisition was performed on a scanning electron microscope (Ultra Plus; Zeiss) at a voxel pitch of 9 × 9 x 21 nm, with individual transverse section images of 8,000 × 8,000 pixels, as described previously (Briggman et al., 2011). The electrons' landing energy was 2.1 keV, the dwell time 200 ns, and the beam current 1 nA, resulting in an electron dose of 15.4 e^{-}/nm^{2}. Image alignment was performed using the Linear Stack Alignment with SIFT (Saalfeld and Tomancák, 2008) plugin for ImageJ (NIH).

Neuron Reconstruction

Manual EM image analysis was performed either by a team of trained students using the KNOSSOS reconstruction tool (https://knossostool.org) or outsourced (ariadne-service, http://www.ariadne-service.ch). Annotators at ariadne-service used the PyKnossos annotation software (Wanner et al., 2016). Each MN was reconstructed three times independently from seed points placed in the axons in a VR, each CoBL was reconstructed three times independently from synaptic locations onto two different MNs (MNs 1 and 42), and each CiD was traced three times independently from seed points placed in somata, after an initial single tracing to exclude common and easily identified non-CiDs (glia, MNs, commissural cells). Discrepancies were resolved either manually by a fourth annotator or by a reannotation algorithm described below.

Resolving Discrepancies between Redundant Annotations

An iterative approach to discrepancy resolution was used. Whenever only one of the independent tracings continued while the others ended, a seed was placed at that location. A different annotator, who did not have access to the previous annotations, was instructed to trace from this seed. This process was iterated, ensuring that every location in a skeleton had been identified by at least two independent annotators.

Processing and Presentation of Data

All processing on skeleton files was performed using custom Python (https://www.python.org) code based on the scipy, numpy (https://www.scipy.org), and networkx (Hagberg et al., 2008) Python libraries. Plots and three-dimensional renderings were made using custom Python code based on matplotlib (Hunter, 2007) and Mayavi (Ramachandran and Varoquaux, 2011).

Quantification of Neuron Locations and Morphologies

Normalized soma positions were calculated by projecting the soma center (the center of mass of points on the soma surface) onto manually defined left-right and D-V axes placed every 12.5 μm along the rostro-caudal extent of the dataset, which takes into account local differences in sample rotation and shape.

Soma sizes were calculated from contours drawn every 250 nm in transverse sections, from which the volumes were calculated. Sizes are reported as the diameter of a sphere of equal volume.

Neurite density contour plots were generated from normalized two-dimensional histograms of the skeleton path length projected onto the appropriate plane.

Gaussian Mixture Model of MN Soma Size Distribution

The distribution of MN soma sizes was fitted using a Gaussian mixture model, using custom Python code based on the scikit-learn library. The number of components was three, based on the Bayesian information criterion (Pedregosa et al., 2011).

Identification of Synapses and Measurement of Synapse Size

Synapses between two neurons were detected by visually inspecting all locations where the two skeletons were closer than 1 μm. Such a (proximity) location was classified as a synaptic contact if two independent annotators confirmed that (1) the two neurons touched each other, (2) a synaptic cleft and (3) an electron-dense thickening were present, and (4) a cluster of vesicles was observed on the presynaptic side in the immediate vicinity of the area of contact between the neurons. Locations where only one annotator detected a synapse were reinspected by a third annotator. The size of a synapse was measured by labeling the complete synaptic contact area in three dimensions. The total synaptic contact area summed over all contacts between an IN and an MN was correlated with the number of contacts between these cells (Figure S4). However, because the synaptic area of a contact is a measure for its synaptic strength (Schikorski and Stevens, 1997; Matsuzaki et al., 2001), we preferred the summed synaptic contact area between an IN and an MN as an indicator of connection strength.

Calculation of the TSI

The TSI was calculated as $(L - M)/(L + M)$, where L and M can stand for (1) the summed synaptic contact area (Figures 5A–5E and 7A–7E), (2) the synapse count (Figures 5E and 7E), or (3) the count of neurite proximity locations (Figures 5D, 5E, 7D, and 7E), between an IN and MNs of the large (L) or medium (M) type.

Statistical Methods

Differences in population means were tested for significance using Student's t test in the case of two populations and the Kruskal-Wallis test followed by Tukey's honestly significant difference (HSD) test in the case of more than two populations. Linear correlations were quantified and tested for significance using Pearson's correlation coefficient. Differences between distributions were tested for significance using the Kolmogorov-Smirnov (KS) test.

SUPPLEMENTAL INFORMATION

Supplemental Information includes four figures, four tables, and three data files and can be found with this article online at https://doi.org/10.1016/j.celrep.2018.05.023.

ACKNOWLEDGMENTS

We thank J. Tritthardt, N. Neef, M. Lukat, A. Scherbarth, M. Kaiser, M. Hilpert, C. Roome, and T. Stather for expert technical help; K.L. Briggman and S.K. Mikula for help with staining procedures; J. Kuhl for help with figure preparation; D. McLean for sharing data on motoneuron input resistance; N. Pfeiler, M.-T. Nguyen, A. Knecht, O. Shatz, A. Stepanov, and M. Pronkin for help with Knossos programming; L.-M. Schreiber, J.H. Youm, H. Jakobi, M. Grohmann, C. Röhrig, A. Gable, and A. Biasotto for help administering the annotator team; S. Mikula, S.K. Mikula, C. Trivedi, S. Preuss, J.-P. Gabriel, and B. Titze for helpful discussions; and the Max Planck Society for financial support. F.N.S. and J.K. thank Boehringer Ingelheim Fonds and J.H.B. Deutsche Forschungsgemeinschaft (DFG) (BO3746/2-1) for financial support.

AUTHOR CONTRIBUTIONS

Conceptualization, F.N.S., W.D., and J.H.B.; Methodology, F.N.S. and W.D.; Software, F.N.S. and J.K.; Formal Analysis, F.N.S., W.D., and J.H.B.; Investigation, F.N.S.; Data Curation, F.N.S.; Funding Acquisition, W.D.; Writing – Original Draft, F.N.S., W.D., and J.H.B.; Writing – Review & Editing, F.N.S., W.D., and J.H.B.; Supervision, W.D. and J.H.B.

DECLARATION OF INTERESTS

F.N.S. and J.K. are shareholders in ariadne-service GmbH.

Received: November 5, 2017
Revised: March 13, 2018
Accepted: May 7, 2018
Published: June 5, 2018

REFERENCES

Ampatzis, K., Song, J., Ausborn, J., and El Manira, A. (2013). Pattern of innervation and recruitment of different classes of motoneurons in adult zebrafish. J. Neurosci. *33*, 10875–10886.

Ampatzis, K., Song, J., Ausborn, J., and El Manira, A. (2014). Separate microcircuit modules of distinct v2a interneurons and motoneurons control the speed of locomotion. Neuron *83*, 934–943.

Asakawa, K., Abe, G., and Kawakami, K. (2013). Cellular dissection of the spinal cord motor column by BAC transgenesis and gene trapping in zebrafish. Front. Neural Circuits *7*, 100.

Bernhardt, R.R., Chitnis, A.B., Lindamer, L., and Kuwada, J.Y. (1990). Identification of spinal neurons in the embryonic and larval zebrafish. J. Comp. Neurol. *302*, 603–616.

Bianco, I.H., Kampff, A.R., and Engert, F. (2011). Prey capture behavior evoked by simple visual stimuli in larval zebrafish. Front. Syst. Neurosci. *5*, 101.

Briggman, K.L., Helmstaedter, M., and Denk, W. (2011). Wiring specificity in the direction-selectivity circuit of the retina. Nature *471*, 183–188.

Burgess, H.A., and Granato, M. (2007). Sensorimotor gating in larval zebrafish. J. Neurosci. *27*, 4984–4994.

Burke, R.E. (1979). The role of synaptic organization in the control of motor unit activity during movement. Prog. Brain Res. *50*, 61–67.

Burke, R.E., Dum, R.P., Fleshman, J.W., Glenn, L.L., Lev-Tov, A., O'Donovan, M.J., and Pinter, M.J. (1982). A HRP study of the relation between cell size and motor unit type in cat ankle extensor motoneurons. J. Comp. Neurol. *209*, 17–28.

Buss, R.R., and Drapeau, P. (2001). Synaptic drive to motoneurons during fictive swimming in the developing zebrafish. J. Neurophysiol. *86*, 197–210.

Cragg, B. (1980). Preservation of extracellular space during fixation of the brain for electron microscopy. Tissue Cell *12*, 63–72.

Denk, W., and Horstmann, H. (2004). Serial block-face scanning electron microscopy to reconstruct three-dimensional tissue nanostructure. PLoS Biol. *2*, e329.

Denny-Brown, D., and Pennybacker, J.B. (1938). Fibrillation and fasciculation in voluntary muscle. Brain *61*, 311–334.

Dougherty, K.J., and Kiehn, O. (2010). Firing and cellular properties of V2a interneurons in the rodent spinal cord. J. Neurosci. *30*, 24–37.

Eklöf-Ljunggren, E., Haupt, S., Ausborn, J., Dehnisch, I., Uhlén, P., Higashijima, S., and El Manira, A. (2012). Origin of excitation underlying locomotion in the spinal circuit of zebrafish. Proc. Natl. Acad. Sci. U S A *109*, 5511–5516.

Fleshman, J.W., Munson, J.B., Sypert, G.W., and Friedman, W.A. (1981). Rheobase, input resistance, and motor-unit type in medial gastrocnemius motoneurons in the cat. J. Neurophysiol. *46*, 1326–1338.

Goulding, M. (2009). Circuits controlling vertebrate locomotion: moving in a new direction. Nat. Rev. Neurosci. *10*, 507–518.

Grillner, S. (2006). Biological pattern generation: the cellular and computational logic of networks in motion. Neuron *52*, 751–766.

Gustafsson, B., and Pinter, M.J. (1984). An investigation of threshold properties among cat spinal alpha-motoneurones. J. Physiol. *357*, 453–483.

Hagberg, A.A., Schult, D.A., and Swart, P. (2008). Exploring network structure, dynamics, and function using NetworkX. In Proceedings of the 7th Python in Science Conference (SciPy 2008), T.V.G. Varoquaux and J. Millman, eds.

Hale, M.E., Ritter, D.A., and Fetcho, J.R. (2001). A confocal study of spinal interneurons in living larval zebrafish. J. Comp. Neurol. *437*, 1–16.

Henneman, E., Somjen, G., and Carpenter, D.O. (1965). Functional significance of cell size in spinal motoneurons. J. Neurophysiol. *28*, 560–580.

Hildebrand, D.G.C., Cicconet, M., Torres, R.M., Choi, W., Quan, T.M., Moon, J., Wetzel, A.W., Scott Champion, A., Graham, B.J., Randlett, O., et al. (2017). Whole-brain serial-section electron microscopy in larval zebrafish. Nature *545*, 345–349.

Hunter, J.D. (2007). Matplotlib: a 2D graphics environment. Comput. Sci. Eng. *9*, 90–95.

Kanda, K., Burke, R.E., and Walmsley, B. (1977). Differential control of fast and slow twitch motor units in the decerebrate cat. Exp. Brain Res. *29*, 57–74.

Kiehn, O. (2016). Decoding the organization of spinal circuits that control locomotion. Nat. Rev. Neurosci. *17*, 224–238.

Kimura, Y., Okamura, Y., and Higashijima, S. (2006). alx, a zebrafish homolog of Chx10, marks ipsilateral descending excitatory interneurons that participate in the regulation of spinal locomotor circuits. J. Neurosci. *26*, 5684–5697.

Kishore, S., Bagnall, M.W., and McLean, D.L. (2014). Systematic shifts in the balance of excitation and inhibition coordinate the activity of axial motor pools at different speeds of locomotion. J. Neurosci. *34*, 14046–14054.

Liao, J.C., and Fetcho, J.R. (2008). Shared versus specialized glycinergic spinal interneurons in axial motor circuits of larval zebrafish. J. Neurosci. *28*, 12982–12992.

Lister, J.A., Robertson, C.P., Lepage, T., Johnson, S.L., and Raible, D.W. (1999). nacre encodes a zebrafish microphthalmia-related protein that regulates neural-crest-derived pigment cell fate. Development *126*, 3757–3767.

Ljunggren, E.E., Haupt, S., Ausborn, J., Ampatzis, K., and El Manira, A. (2014). Optogenetic activation of excitatory premotor interneurons is sufficient to generate coordinated locomotor activity in larval zebrafish. J. Neurosci. *34*, 134–139.

Marques, J.C., Lackner, S., Felix, R., and Orger, M.B. (2018). Structure of the zebrafish locomotor repertoire revealed with unsupervised behavioral clustering. Curr. Biol. *28*, 181–195.5.

Masino, M.A., and Fetcho, J.R. (2005). Fictive swimming motor patterns in wild type and mutant larval zebrafish. J. Neurophysiol. *93*, 3177–3188.

Matsuzaki, M., Ellis-Davies, G.C.R., Nemoto, T., Miyashita, Y., Iino, M., and Kasai, H. (2001). Dendritic spine geometry is critical for AMPA receptor expression in hippocampal CA1 pyramidal neurons. Nat. Neurosci. *4*, 1086–1092.

McElligott, M.B., and O'Malley, D.M. (2005). Prey tracking by larval zebrafish: axial kinematics and visual control. Brain Behav. Evol. *66*, 177–196.

McLean, D.L., and Dougherty, K.J. (2015). Peeling back the layers of locomotor control in the spinal cord. Curr. Opin. Neurobiol. *33*, 63–70.

McLean, D.L., Fan, J., Higashijima, S., Hale, M.E., and Fetcho, J.R. (2007). A topographic map of recruitment in spinal cord. Nature *446*, 71–75.

McLean, D.L., Masino, M.A., Koh, I.Y., Lindquist, W.B., and Fetcho, J.R. (2008). Continuous shifts in the active set of spinal interneurons during changes in locomotor speed. Nat. Neurosci. *11*, 1419–1429.

Menelaou, E., and McLean, D.L. (2012). A gradient in endogenous rhythmicity and oscillatory drive matches recruitment order in an axial motor pool. J. Neurosci. *32*, 10925–10939.

Menelaou, E., VanDunk, C., and McLean, D.L. (2014). Differences in the morphology of spinal V2a neurons reflect their recruitment order during swimming in larval zebrafish. J. Comp. Neurol. *522*, 1232–1248.

Myers, P.Z., Eisen, J.S., and Westerfield, M. (1986). Development and axonal outgrowth of identified motoneurons in the zebrafish. J. Neurosci. *6*, 2278–2289.

Pedregosa, F., Varoquaux, G., Gramfort, A., Michel, V., Thirion, B., Grisel, O., Blondel, M., Prettenhofer, P., Weiss, R., Dubourg, V., et al. (2011). Scikit-learn: machine learning in Python. J. Mach. Learn. Res. *12*, 2825–2830.

Ramachandran, P., and Varoquaux, G. (2011). Mayavi: 3D visualization of scientific data. Comput. Sci. Eng. *13*, 40–50.

Ritter, D.A., Bhatt, D.H., and Fetcho, J.R. (2001). In vivo imaging of zebrafish reveals differences in the spinal networks for escape and swimming movements. J. Neurosci. *21*, 8956–8965.

Roberts, A., Li, W.C., and Soffe, S.R. (2010). How neurons generate behavior in a hatchling amphibian tadpole: an outline. Front. Behav. Neurosci. *4*, 16.

Saalfeld, S., and Tomancák, P. (2008). Automatic landmark correspondence detection for ImageJ. In Proceedings of the ImageJ User and Developer Conference, pp. 128–133.

Satou, C., Kimura, Y., Kohashi, T., Horikawa, K., Takeda, H., Oda, Y., and Higashijima, S. (2009). Functional role of a specialized class of spinal commissural inhibitory neurons during fast escapes in zebrafish. J. Neurosci. *29*, 6780–6793.

Satou, C., Kimura, Y., and Higashijima, S. (2012). Generation of multiple classes of V0 neurons in zebrafish spinal cord: progenitor heterogeneity and temporal control of neuronal diversity. J. Neurosci. *32*, 1771–1783.

Satou, C., Kimura, Y., Hirata, H., Suster, M.L., Kawakami, K., and Higashijima, S. (2013). Transgenic tools to characterize neuronal properties of discrete populations of zebrafish neurons. Development *140*, 3927–3931.

Schikorski, T., and Stevens, C.F. (1997). Quantitative ultrastructural analysis of hippocampal excitatory synapses. J. Neurosci. *17*, 5858–5867.

Song, J., Ampatzis, K., Björnfors, E.R., and El Manira, A. (2016). Motor neurons control locomotor circuit function retrogradely via gap junctions. Nature *529*, 399–402.

Stepien, A.E., Tripodi, M., and Arber, S. (2010). Monosynaptic rabies virus reveals premotor network organization and synaptic specificity of cholinergic partition cells. Neuron *68*, 456–472.

Sternberg, J.R., Severi, K.E., Fidelin, K., Gomez, J., Ihara, H., Alcheikh, Y., Hubbard, J.M., Kawakami, K., Suster, M., and Wyart, C. (2016). Optimization of a neurotoxin to investigate the contribution of excitatory interneurons to speed modulation in vivo. Curr. Biol. *26*, 2319–2328.

Trivedi, C.A., and Bollmann, J.H. (2013). Visually driven chaining of elementary swim patterns into a goal-directed motor sequence: a virtual reality study of zebrafish prey capture. Front. Neural Circuits *7*, 86.

Ulfhake, B., and Kellerth, J.-O. (1982). Does α-motoneurone size correlate with motor unit type in cat triceps surae? Brain Res. *251*, 201–209.

van Raamsdonk, W., Mos, W., Smit-Onel, M.J., van der Laarse, W.J., and Fehres, R. (1983). The development of the spinal motor column in relation to the myotomal muscle fibers in the zebrafish (Brachydanio rerio). I. Posthatching development. Anat. Embryol. (Berl.) *167*, 125–139.

Wanner, A.A., Genoud, C., Masudi, T., Siksou, L., and Friedrich, R.W. (2016). Dense EM-based reconstruction of the interglomerular projectome in the zebrafish olfactory bulb. Nat. Neurosci. *19*, 816–825.

Wyart, C., Del Bene, F., Warp, E., Scott, E.K., Trauner, D., Baier, H., and Isacoff, E.Y. (2009). Optogenetic dissection of a behavioural module in the vertebrate spinal cord. Nature *461*, 407–410.

Zajac, F.E., and Faden, J.S. (1985). Relationship among recruitment order, axonal conduction velocity, and muscle-unit properties of type-identified motor units in cat plantaris muscle. J. Neurophysiol. *53*, 1303–1322.